Article

The Effect of Counterions on the Detection of Cu²⁺ Ions in Aqueous Solutions Using Quartz Tuning Fork (QTF) Sensors Modified with L-Cysteine Self-Assembled Monolayers: Experimental and Quantum Chemical DFT Study

Shofiur Rahman [1,*], Mahmoud A. Al-Gawati [1,2], Fatimah S. Alfaifi [2], Muthumareeswaran Muthuramamoorthy [1], Amal F. Alanazi [3], Hamad Albrithen [1,2], Khalid E. Alzahrani [1,2], Abdulaziz K. Assaifan [1,4], Abdullah N. Alodhayb [1,2,*] and Paris E. Georghiou [5,*]

[1] Biological and Environmental Sensing Research Unit, King Abdullah Institute for Nanotechnology, King Saud University, P.O. Box 2455, Riyadh 11451, Saudi Arabia

[2] Department of Physics and Astronomy, College of Science, King Saud University, Riyadh 11451, Saudi Arabia

[3] Energy, Water, and Environment Lab, Faculty of Humanities and Sciences, Prince Sultan University, Riyadh 11586, Saudi Arabia

[4] Department of Biomedical Technology, College of Applied Medical Sciences, King Saud University, Riyadh 11451, Saudi Arabia

[5] Department of Chemistry, Memorial University of Newfoundland, St. John's, NL A1B 3X7, Canada

* Correspondence: mrahman1@ksu.edu.sa (S.R.); aalodhayb@ksu.edu.sa (A.N.A.); parisg@mun.ca (P.E.G.)

Abstract: In this study, a sensing device employing a gold-coated quartz tuning fork (QTF) modified with a self-assembled monolayer (SAM) of L-cysteine was evaluated for the sensitive detection of Cu^{2+} ions in aqueous solutions. Three copper (II) salts, $CuSO_4$, $CuCl_2$, and $Cu(NO_3)_2$, at four different concentrations (10^{-12}, 10^{-10}, 10^{-8}, and 10^{-6} M) in small (100 μL) water sample amounts were each used as analytes to investigate the influence of their counterions in the detection of the Cu^{2+} ions. It was found that, among the counterions, the sulfate anion had the largest effect upon the detection of Cu^{2+} in water, in the following order: $SO_4^{2-} > Cl^- > NO_3^-$. The lower limit of detection of the Cu^{2+} ions detected was in the 10^{-12} M range. The frequency shifts measured with the QTFs relative to deionized water were inversely proportional to the concentration/mass of the analytes. Density functional theory calculations were conducted to understand the effect of the counterions on the respective electronic interaction energies for the apparent host–guest binding of the analytes with L-cysteine and with gold surface-bound L-cysteine molecules. Gas phase (both with and uncorrected BSSE) and solution phase interaction energies (ΔIE) calculated at the B3LYP/LANL2DZ and ωB97XD levels of theory showed that the stability for the complexes were in the following order: [L-cysteine]⊃[CuSO₄] > [L-cysteine]⊃[CuCl₂] > [L-cysteine]⊃[Cu(NO₃)₂], which supports our experimental findings, as they were in the same order as the experimentally observed order for the copper salts tested: $CuSO_4 > CuCl_2 > Cu(NO_3)_2$.

Keywords: quartz tuning fork; L-cysteine; self-assembled monolayer; anions effect; density functional theory

1. Introduction

Most proteins contain the amino acid L-cysteine (LC). LC is soluble and zwitterionic in water, is biocompatible, and is useful as a chelating ligand for several heavy metal ions [1]. LC has three potential metal-binding groups that can act as a monodentate, a bidentate, or a tridentate ligand since it can present a nucleophilic thiolate, an amino, and/or a carboxylate group to metal centers. The coordination of LC is highly dependent on both the type of metal ions and the surroundings of the interaction(s). The thiolate and amine/carboxyl

groups are classified as soft and hard bases, respectively, using Pearson's HSAB theory, and can coordinate with hard or soft metal ions [2,3].

Self-assembled monolayers (SAMs) of thiols on gold (Au) surfaces are among the most widely used model systems for researching the self-assembly of organic molecule onto metal surfaces. In the fields of chemistry, physics, molecular biology, pharmaceutical engineering, and materials science, SAMs based on thiol–gold chemistry have been extensively used [4–6]. The strength of the gold–sulfur (Au–S) interaction formed between thiols and Au surfaces provides the basis to fabricate robust SAMs for diverse applications. Zhang et al. reported the nature of Au–S interactions and the stability of SAMs formed on Au surfaces under various conditions, which include the different surface properties of the Au, the solution pHs, and the nature of solvents used [7]. In their study, they reported that the thiol groups formed SAMs with gold via a monodentate stable covalent bond.

After iron and zinc, copper is the third most ubiquitous of the transition metal ions, which play important roles in human health and have a significant impact on the body. Copper ion also serves as a catalytic center in many enzymes and is utilized in biological processes including respiration, the production of cellular energy, and the removal of reactive oxygen substances [8–10]. A deficiency in Cu^{2+} ions may alter the body's ability to use some of its enzymes, which can result in a range of neurological issues, while an excess of Cu^{2+} ions may harm the kidneys and liver. The metabolism of copper in an organism is strictly controlled, and its disturbance results in several illnesses, including Wilson [11] and Menkes [12] disorders, which also contribute to the development of cancer [13], inflammation [14], and neurological conditions [15] such as Alzheimer's disease.

Therefore, developing an efficient, high-performance, and environmentally friendly technique that allows for the ultrasensitive and precise detection of Cu^{2+} ions is essential. Several analytical techniques have been used to quantify the concentration of the Cu^{2+} ions at trace levels, including ultrasensitive fluorescence spectrometry [16], surface-enhanced Raman spectroscopy [17], inductively coupled plasma optical emission spectrometry (ICP-OES), flame atomic absorption spectrometry (F-AAS) [18], and reflectance spectrometry [19]. Although many of these methods have excellent detection limits and are capable of multi-element analysis, they also have some limitations when it comes to precisely detecting trace amounts of Cu^{2+} ions. These limitations include expensive equipment facilities, knowledgeable and skilled personnel, and time-consuming and complex sample preparation.

As one the best platforms for sensing analyte metal ions, SAMs on the surface of metal electrodes have been explored through binding with the functional groups present in the backbone and on the surface of SAMs [4–6]. Surface acoustic wave [20], quartz crystal microbalance [21], and microcantilever sensors [22–30] are examples of modern chemosensing devices that exhibit exceptional sensitivity to target analytes. In recent years, we have developed and evaluated suitably functionalized calix [4] arenes metal-detecting layers on sensitive microcantilevers (MCLs). We found that both the cation and their counterions significantly contributed to the MCL responses when aqueous solutions of metal ions interacted with the calix [4] arene-modified MCLs [24–28].

One of the most recent developments in chemical sensing technology is the use of quartz tuning forks (QTFs). QTFs are made using the piezoelectric material silicon dioxide (SiO_2) and are frequently used as a sensitive detector in many fields, including atomic force microscopy, scanning near-field optical microscopy, femto-Newtonian force sensing, alternating gradient magnetometry, magnetic force microscopy, and for the detection of electric field intensity distribution [31–36]. Günther et al. employed QTFs for scanning near-field acoustic microscopy (NSAM) very early on in the evolution of scanning probe microscopy [34]. QTFs consist of two vibrating prongs with a high-quality (Q) factor that has high mechanical and thermal stability, low cost and power consumption, employs a simple operating circuit system, and has a fast response time [36]. In addition, minute samples can be tested.

Recently, we reported on gold-coated QTFs surface functionalized with the SAMs of L-cysteine (LC) and L−glutathione for the detection of aqueous solutions of $CaCl_2$,

$HgCl_2$, and $PbCl_2$ using chemical host–guest interactions [37]. The LC molecules bond onto the gold surface via their thiol (SH) functional group. The formation of the SAMs of the LC on the gold surface was confirmed using X-ray photoelectron spectroscopy (XPS) [37] and attenuated total reflectance Fourier transform infrared spectroscopy (ATR-FTIR) [38]. According to the Hofmeister series, the strength of anions is often ordered as follows: $F^- \approx SO_4^{2-} > HPO_4^{2-} > CH_3COO^- > Cl^- > NO_3^- > Br^- > ClO_3^- > I^- > ClO_4^- > SCN^-$. The significant role of the Hofmeister effect in a wide range of biological and physicochemical phenomena has been extensively and experimentally confirmed over the last century. To the best of our knowledge, a combined analysis of a theoretical quantum chemical study and an ultrasensitive QTF sensing experiment that addresses the counterion effect for the interactions of LC with aqueous solutions of divalent copper salts such as $CuSO_4$, $CuCl_2$, and $Cu(NO_3)_2$ has not yet been reported in the literature.

As a follow-up to our recent work [37] on QTF sensing systems, we now report on a LC-modified SAM on a Au-coated QTFs sensing device which has been used for the sensitive detection of Cu^{2+} ions in the aqueous solutions of its salts and the effects of their respective SO_4^{2-}, Cl^-, and NO_3^- counter ions.

2. Materials and Experimental Details

2.1. Chemicals and Materials

L-cysteine, copper (II) sulfate ($CuSO_4$, anhydrous, 99.99%); cupric (I) chloride dihydrate ($CuCl_2 \cdot 2H_2O$, 99%), copper (II) nitrate trihydrate ($Cu(NO_3)_2 \cdot 3H_2O$ 98%), dichloromethane, and ethanol were procured from Sigma–Aldrich, Burlington, MA, USA. All aqueous solutions were prepared using deionized (DI) water with a resistivity of 18.6 MΩ·cm. The pH of the deionized water was 6.82. The pH value of the analyte solutions was 6.85.

The Au–coated QTFs were purchased from Forien Inc., Edmonton, AB, Canada. They were coated with Au using a vacuum evaporation method; the thickness of the gold coating was around 100 nm. The resonance frequency of the QTFs was 32.768 kHz, the spring constant was ~20 kN/m, and the load capacitance was 12.5 pF. A 10^{-6} M solution of LC was used to functionalize the Au-coated QTFs.

2.2. Experimental Setup and Instrumentation

QTF resonance frequencies were measured using a Quester Q10 (Fourien Inc., Edmonton, AB, Canada) instrument. The Quester Q10 consists of an integrated impedance analyzer which can perform frequency sweeps, as well as measure the real and imaginary components of the impedance response. To resonate the QTFs at fixed frequencies, the proportional integrated differential technique was used in this system. When coupled with a translation stage, the system can be used to maintain the distance between the QTF and any given analyte solute. The output measured data were analyzed using MATLAB or the Origin Lab program. Figure 1 shows a schematic illustration of the LC-SAM functionalized Au-coated QTFs system. A detailed instrumental setup of the system and software integration can be found in our previous study and elsewhere [36].

2.3. Experimental Methods

Au-coated QTFs were immersed in a solution of LC (10^{-6} M in DI water) for 1 h to prepare the SAMs. These activated QTFs were used to determine the resonance frequency at four different concentrations (10^{-12}, 10^{-10}, 10^{-8}, and 10^{-6} M) of each of the analytes ($CuSO_4$, $CuCl_2$, and $Cu(NO_3)_2$). To ensure that all experiments were performed under consistent conditions, the QTFs were immersed directly at a constant depth of 25 µm into a small droplet of volume 100 µL) of the respective analyte solutions.
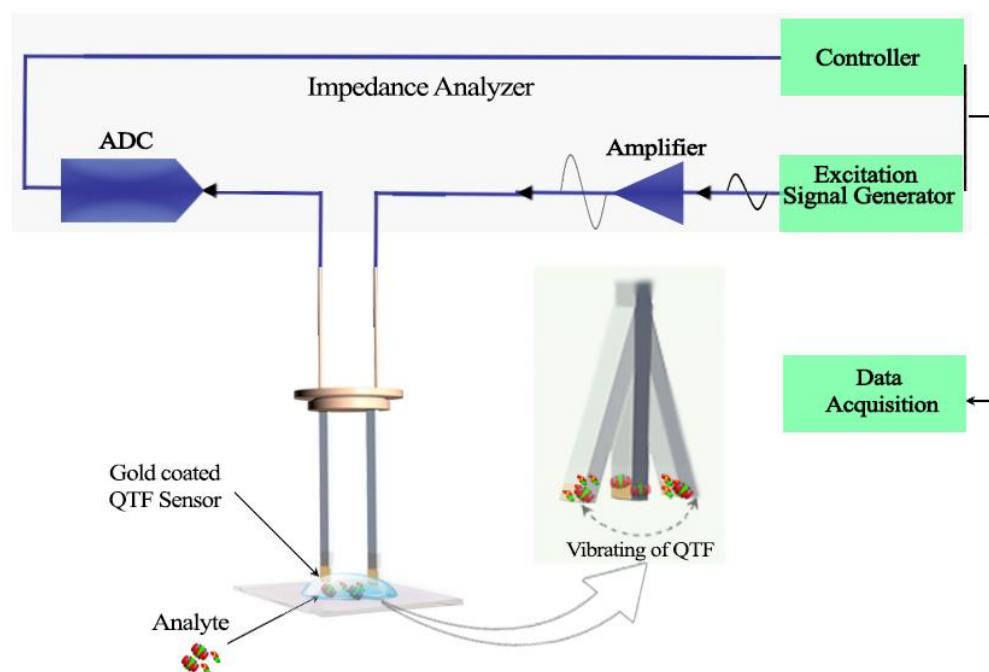
Figure 1. Schematical illustration of the QTF measurement system used.

2.4. Density Functional Theory (DFT) Calculations

To visualize the nature of the noncovalent interactions of LC with each of the three analytes, single-point density functional theory (DFT) calculations were performed at both the B3LYP/LANL2DZ and ωB97XD/LANL2DZ levels of theory. The initial molecular geometries of all the examined compounds were drawn using the *GaussView 6.0.16* program [39]. All DFT calculations were first conducted using *Gaussian 16, Revision C.01* [40] in the gas phase, and then the optimized structures were further computed with a water solvent system using the polarized continuum model (PCM). A vibrational analysis was carried out for each optimized molecule to ensure that they were in a vibrational energy minimum and had no imaginary frequencies. Molecular electrostatic potential (MEP) maps were also visualized using *GaussView 6.0.16*. Additionally, the counterpoise (CP) corrections were also calculated to remove the basis set superposition errors (BSSEs) [41,42] for the noncovalent intermolecular interactions between the LC and analytes ($CuSO_4$, $CuCl_2$, and $Cu(NO_3)_2$).

The electronic interaction energy (ΔE_{int} kJ mole^{-1}) and Gibbs interaction energy (ΔG_{int} kJ mole^{-1}) values were calculated using Equations (1)–(4) for the components of the hypothetical modeled complexes formed by the LC and LC-Au with the respective analytes, as shown in Figure 2, and which is discussed in further detail in Section 3.2.

$$\Delta E_{int} \text{ for } LC \supset analyte = E_{[LC] \supset [analyte]} - (E_{[LC]} + E_{[analyte]}) \tag{1}$$

$$\Delta E_{int} \text{ for } LC\text{-}Au \supset analyte = E_{[LC\text{-}Au] \supset [analyte]} - (E_{[LC\text{-}Au]} + E_{[analyte]}) \tag{2}$$

where $E_{[LC] \supset [analyte]}$ = optimized energy of the LC complex(es) with each of the analytes; $E_{[LC]}$ = optimized electronic energy of the free LC; $E_{[LC\text{-}Au] \supset [analyte]}$ = optimized energy of the [LC-Au] complex(es) with analytes; $E_{[LC\text{-}Au]}$ = optimized electronic energy of the [LC-Au]; and $E_{[analyte]}$ = optimized electronic energy of the individual Cu^{2+} analyte salts.

$$\Delta G_{int} \text{ for } LC \supset analyte = G_{[LC] \supset [analyte]} - (G_{[LC]} + E_{[analyte]}) \tag{3}$$

$$\Delta G_{int} \text{ } LC\text{-}Au \supset analyte = E_{[LC\text{-}Au] \supset [analyte]} - (E_{[LC\text{-}Au]} + E_{[analyte]}) \tag{4}$$
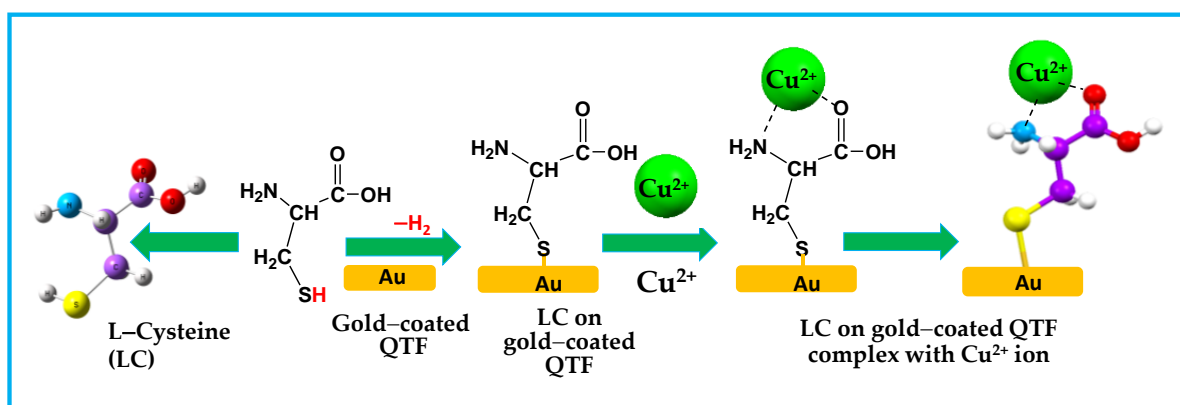
Figure 2. Proposed binding mode of the LC on Au-coated-QTF complex with Cu^{2+} ions (counterion not shown). Color code: carbon = purple, nitrogen = blue; oxygen = red; copper = green; sulfur = yellow; gold = orange and hydrogen atoms = white.

3. Results and Discussion

3.1. Resonance Frequency Measurements of Au-Coated QTFs Functionalized with L-Cysteine at the Different Concentrations of CuSO$_4$, CuCl$_2$, and Cu(NO$_3$)$_2$

All experiments were conducted at four different concentrations (10^{-12}, 10^{-10}, 10^{-8}, and 10^{-6} M) of each or the three Cu^{2+} salts using Au-coated QTFs with and without LC SAM coating. All measurements were conducted in triplicate. QTF sensor measurements were performed between each solute measurement with a drop of Milli-Q water as control experiments. Additionally, measurements were also conducted using non-LC functionalized Au-coated QTFs to confirm that there were no frequency changes, thus indicating that no interactions of the Cu^{2+} ions occurred with the Au-coated QTFs surfaces alone. In our previous study, we showed that, by using LC Au-coated QTFs with a higher quality factor resonance frequency, concentrations of aqueous calcium ions in CaCl$_2$ and HgCl$_2$ salts as low as 10^{-12} M could be determined [37].

As with our previous study, the QTFs were immersed in 100 µL amounts of the analyte solutions and the controls, and the time used for each sample measurement was maintained for approximately 2 min at room temperature. The frequency of the QTF was swept from 30,900 to 35,000 Hz using the software control of the system, and each cycle was completed in a maximum of approximately 30 s.

In general, the resonance frequency shift (Δf) of a QTF is dependent on a change in mass loading (Δm) and effective stiffness (Δk) of a given solute, as shown in Equation (5) [37], where f_0, k_0, and m_0 are the resonance frequency, spring constant, and mass of the functionalized QTF, respectively:

$$\Delta f = \left(\frac{f_0}{2} \right) \left(\frac{\Delta k}{k_0} - \frac{\Delta m}{m_0} \right) \tag{5}$$

Figure 3a–d show the comparison of resonance frequency responses of the LC functionalized Au-coated QTFs when immersed in the different concentrations (10^{-12} to 10^{-6} M) of the three analytes, and the results are summarized in Table 1.
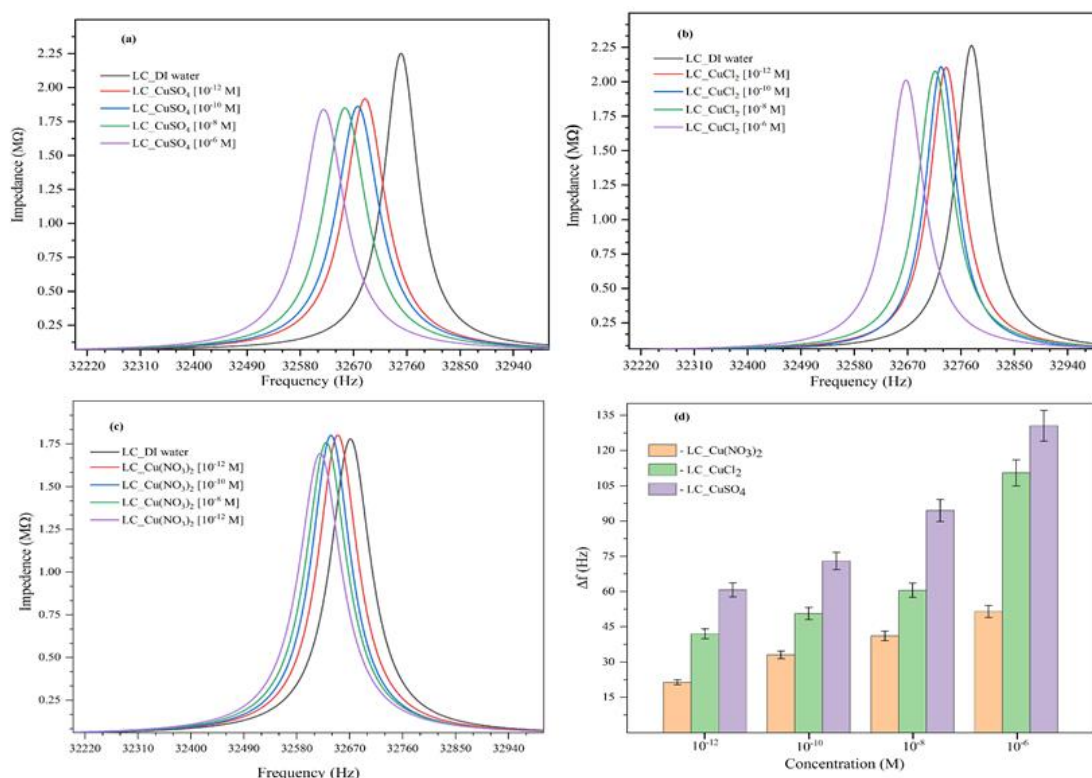
Figure 3. Comparison of the resonance frequency responses of the Au-coated QTFs functionalized with LC with the different concentrations (10^{-12} M to 10^{-6} M) of each of the aqueous Cu^{2+} salt solutions: (**a**) $CuSO_4$, (**b**) $CuCl_2$, (**c**) $Cu(NO_3)_2$, and (**d**) summary histogram showing the relative resonance frequency shifts (Δf) +/− ~5% to the three copper salts tested.

Table 1. Comparison of the resonance frequency shift of the LC functionalized Au-coated QTFs in the different analyte concentrations (10^{-12} to 10^{-6} M) of the three analytes.

Analyte Concentration (M)	Resonance Frequency Shift (Hz)		
	$CuSO_4$	$CuCl_2$	$Cu(NO_3)_2$
10^{-12}	60.72 ± 3.34	42.02 ± 2.10	21.36 ± 1.07
10^{-10}	72.99 ± 3.65	50.69 ± 2.53	33.04 ± 1.65
10^{-8}	94.49 ± 4.72	60.51 ± 3.03	41.13 ± 2.06
10^{-6}	130.54 ± 6.53	110.53 ± 5.53	51.52 ± 2.58

The resonance frequency shifts were calculated using Equation (6) and the results are shown in Figure 3d.

$$\Delta f = f_{ref} - f_a \tag{6}$$

where f_{ref} and f_a are the resonance frequency of the distilled water control and the tested analytes at the 10^{-12}, 10^{-10}, 10^{-8}, and 10^{-6} M concentrations.

It is well known that the resonance frequency shift is considered as an important sensor response. From Figure 3, therefore, it can be clearly seen that the resonance frequency positions were shifted downfield with increasing analyte concentrations. This is due to the corresponding mass increases resulting from the host–guest binding of the analytes with the LC molecules of the SAM on the Au-QTF surface [37]. For each of the solutes, a different Au-QTF-LC was used. The resonance frequency shifts of the tested analytes were calculated by subtracting the resonance frequency values from the respective resonance frequency values of the QTF-LC in DI water. Figure 3a shows that the largest resonance frequency shift, Δf = 130.5 Hz, is the decrease in the resonance frequencies from 32,750 Hz

in the DI water to 32,620 Hz after immersion in the aqueous 10^{-6} M $CuSO_4$ solutions, with smaller shifts occurring for the more dilute solutions. Other resonance frequency decreases are also observed for the other analyte solutions, as shown in Figure 3b,c. The resonance frequency shifts for the same concentrations of the different copper solutions relative to DI are summarized and compared in Figure 3d. As can be seen, for the 10^{-6} M solutions of the $CuSO_4$, $CuCl_2$, and $Cu(NO_3)_2$, the shifts were 130, 110, and 52 Hz, respectively. Similar trends can be seen for the other concentrations, including, e.g., 61, 42, 21 Hz, respectively, for the 10^{-12} solutions. The highest resonance frequency shift for the corresponding 10^{-6} M solutions was in the following order: $CuSO_4$ (130.5 Hz) > $CuCl_2$ (110.5 Hz) > $Cu(NO_3)_2$ (51.5 Hz).

It is expected that the mass loading (i.e., concentration) would have had a large impact on the resonance frequency, whereas, from Equation (3), the stiffness of the QTF has a negligible impact. Thus, the frequencies relative to those of the QTFs in the DI water are inversely proportional to the concentration/mass of the analytes on the QTFs-LC surface. The experimental results showed that the counterions examined in this work do have a significant impact upon the responses of the Au-coated QTF-LC sensor used for the detection of Cu^{2+} ions in aqueous solutions. To gain further insight and understand the nature of the electrostatic interactions on the QTF-LC sensors for the analytes, DFT quantum chemical calculations were conducted on the molecular structures of LC and its hypothetical complexes with the different analytes.

3.2. Quantum Chemical DFT Calculations

DFT and quantum chemical calculations [39–46] were conducted to investigate the electrostatic interactions between the QTFs-LC with the three Cu^{2+} salts. We hypothesized that, during the incubation, LC formed a SAM on the coated Au surface of the QTFs by covalent S-Au bond formation. Cu^{2+} ions then bind with the LC by electrostatic noncovalent "host-guest" interactions between the carbonyl and amino groups via a bidentate N,O coordination mode, as depicted in Figure 2. The DFT calculations were conducted in the gas phase and water solvent system for LC and LC-Au with each of the three Cu^{2+} salts at the B3LYP/LANL2DZ and ωB97XD/LANL2DZ level of theory. To simplify the quantum chemical calculations and reduce the computation time, the DFT calculations were conducted using a single molecule of LC and a single molecule of gold attached to the LC (shown as LC-Au). The optimized molecular structures of LC, LC-Au, and their binding modes with the three analytes are shown in Figure 4. The DFT-calculated electronic binding interaction energies (ΔIE kJ mole^{-1}) and free energies (ΔG kJ mole^{-1}) are summarized in Tables 2 and 3. Tables 2 and 3 show the resulting electronic binding interaction energies (ΔIE kJ mole^{-1}) with both uncorrected and corrected BSSE values. Negative ΔIE values correlate with favorable interactions. The BSSE-uncorrected calculated gas phase interaction energies (ΔIE) at the ωB97XD/LANL2DZ level of theory are -292.87, -172.77, and -147.29 kJ mol^{-1} for the [LC]⊃[CuSO$_4$], [LC]⊃[CuCl$_2$], and [LC]⊃[Cu(NO$_3$)$_2$] complexes, respectively, and -267.75, -151.69, and -117.825 kJ mol^{-1} for the respective corresponding BSSE-corrected values. The BSSE-uncorrected calculated gas phase interaction energies (ΔIE) at the ωB97XD/LANL2DZ level of theory are -469.85, -190.82, and -137.48 kJ mol^{-1} for [LC-Au]⊃[CuSO$_4$], [LC-Au]⊃[CuCl$_2$] and [LC-Au]⊃[Cu(NO$_3$)$_2$] complexes, respectively and -288.44, -144.89 and -139.86 kJ mol^{-1} for the respective corresponding BSSE-corrected values. The results from both methods are consistent. The DF-calculated results confirm that $CuSO_4$ has the highest electronic binding interaction and Gibbs interaction energies for the hypothetical 1:1 complexes of LC and LC-Au with the tested analytes in the following order: $CuSO_4$ > $CuCl_2$ > $Cu(NO_3)_2$. The DFT calculated results with both uncorrected and corrected BSSE values are demonstrate that the counterions have a significant influence on the electrostatic interactions involved between the LC/LC-Au and the tested analytes ($CuSO_4$, $CuCl_2$, and $Cu(NO_3)_2$).
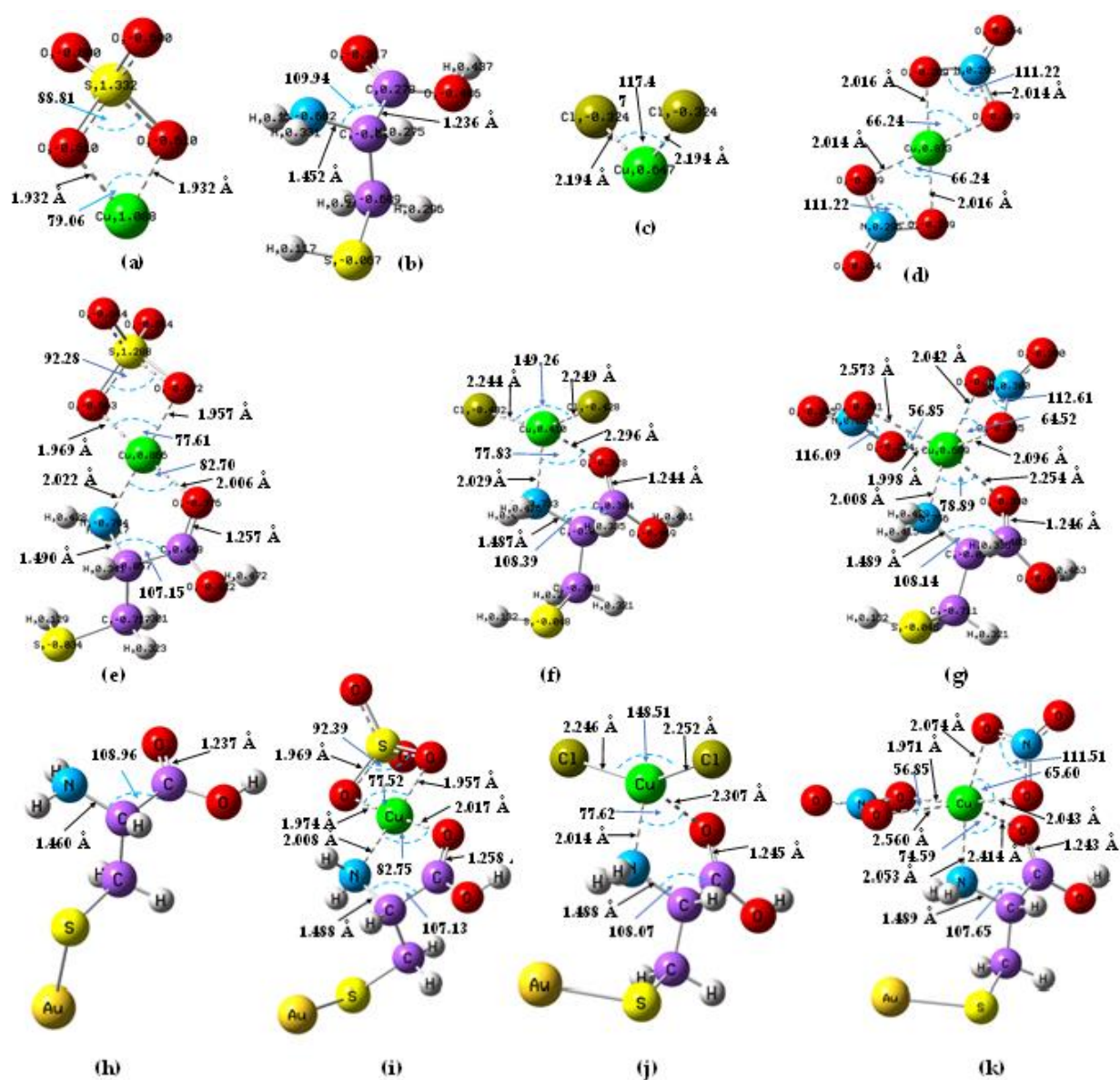
Figure 4. The optimized ball-and-stick molecular structures of (**a**) CuSO$_4$; (**b**) LC; (**c**) CuCl$_2$; (**d**) Cu(NO$_3$)$_2$; (**e**) LC⊃CuSO$_4$; (**f**) LC⊃CuCl$_2$; (**g**) LC⊃Cu(NO$_3$)$_2$; (**h**) [LC-Au]; (**i**) [LC-Au]⊃CuSO$_4$; (**j**) [LC-Au]⊃CuCl$_2$; and (**k**) [LC-Au]⊃Cu(NO$_3$)$_2$ at the ωB97XD/LANL2DZ level of theory in water solvent system. Color code: carbon = purple, nitrogen = blue; oxygen = red; copper = green; chlorine = yellow-green; sulfur = yellow; gold (Au) = orange; and hydrogen atoms = white.

Table 2. Comparison of DFT-calculated gas phase electronic binding interaction energies (ΔIE kJ mol^{-1}) and Gibbs interaction energies (ΔG kJ mol^{-1}) for 1:1 complexes of LC and LC-gold(Au) with $CuSO_4$; $Cu(NO_3)_2$, and $CuCl_2$ at the B3LYP/LANL2DZ and ωB97XD/LANL2DZ levels of theory.

Complex	ΔIE and ΔG (kJ/mole) of the Analytes ($CuSO_4$; $CuCl_2$, and $Cu(NO_3)_2$)							
	B3LYP/LANL2DZ				ωB97XD/LANL2DZ			
	Uncorrected BSSE		Corrected BSSE		Uncorrected BSSE		Corrected BSSE	
	ΔIE	ΔG	ΔIE	ΔG	ΔIE	ΔG	ΔIE	ΔG
[LC] $\supset$ [$CuSO_4$]	−283.98	−217.33	−259.05	−194.00	−292.87	−223.87	−267.75	−201.11
[LC] $\supset$ [$CuCl_2$]	−133.26	−115.71	−112.12	−95.66	−172.77	−112.22	−151.69	−107.41
[LC] $\supset$ [$Cu(NO_3)_2$]	−115.57	−59.82	−86.91	−33.08	−147.29	−88.55	−117.82	−59.45
[LC-Au] $\supset$ [$CuSO_4$]	−299.34	−229.81	−274.01	205.60	−314.05	−243.26	−288.44	−218.96
[LC-Au] $\supset$ [$CuCl_2$]	−143.86	−124.68	−122.29	−104.06	−190.82	−145.04	−144.89	−102.19
[LC-Au]$\supset$[$Cu(NO_3)_2$]	−124.16	−67.75	−97.81	−42.49	−137.48	−120.39	−139.86	−101.80

Table 3. Comparison of DFT-calculated electronic binding interaction energies (ΔIE kJ mol^{-1}) and Gibbs interaction energies (ΔG kJ mol^{-1}) in water solvent system for 1:1 complexes of LC, LC−gold (Au) with $CuSO_4$, $Cu(NO_3)_2$, and $CuCl_2$ at the B3LYP/LANL2DZ and ωB97XD/LANL2DZ levels of theory.

Complex	ΔIE and ΔG (kJ/mole) of the analytes ($CuSO_4$; $CuCl_2$, and $Cu(NO_3)_2$)			
	B3LYP/LANL2DZ		ωB97XD/LANL2DZ	
	ΔIE	ΔG	ΔIE	ΔG
[LC] $\supset$ [$CuSO_4$]	−249.01	−180.097	−268.61	−197.68
[LC] $\supset$ [$CuCl_2$]	−167.57	−112.22	−198.40	−119.17
[LC] $\supset$ [$Cu(NO_3)_2$]	−133.61	−76.68	−177.92	−115.57
[LC-Au] $\supset$ [$CuSO_4$]	−264.58	−195.88	−292.13	−220.17
[LC-Au] $\supset$ [$CuCl_2$]	−143.86	−124.68	−190.82	−145.04
[LC-Au] $\supset$ [$Cu(NO_3)_2$]	−142.77	−85.57	−180.75	−118.98

For the selected atom distances shown in Figure 4 and summarized in Table 4, the average values were determined from the closest contact distances between Cu^{2+} and the oxygen atoms in $CuSO_4$ and $Cu(NO_3)_2$, and between Cu^{2+} and the chloride ions in $CuCl_2$. The distances between Cu^{2+} with the carbonyl oxygen (>C=O) and Cu^{2+} with the nitrogen (−NH$_2$) of the LC are also shown in Figure 4 and summarized in Table 4. The corresponding selected bond angles are summarized in Table 5. The output files for the DFT calculation for all the geometry optimized structures reported can be downloaded at Supplementary Materials.

Table 4. DFT-calculated selected bond distances (in angstroms (Å)) for the selected atoms of LC; LC-Au; $CuSO_4$; $CuSO_4$; $Cu(NO_3)_2$; $CuCl_2$ and their 1:1 complex at the ωB97XD/LANL2DZ level of theory in the water solvent system.

	>HC to NH$_2$ (Å) of LC	>HC to C=O (Å) of LC	Cu to NH$_2$ (Å) of LC	Cu to O=C< (Å) of LC	Cu to >S=O(Å) of $CuSO_4$ (Avg)	Cu to Cl (Å) of $CuCl_2$ (Avg)	Cu to O=N (Å) of $Cu(NO_3)_2$ (Avg)	−C=O..Cu..NH$_2$ (Å) for LC with Cu^{2+} (Avg)	Ionic charge of Cu^{2+}
LC	1.452	1.236	–	–	–	–	–	–	–
LC-Au	1.460	1.237	–	–	–	–	–	–	–
$CuSO_4$	–	–	–	–	1.932	–	–	–	1.088
LC$\supset CuSO_4$	1.490	1.256	2.022	2.006	11.963	–	–	2.014	0.866
[LC-Au] $\supset CuSO_4$	1.488	1.258	2.008	2.017	1.965	–	–	2.012	0.858
$CuCl_2$	–	–	–	–	–	2.194	–	–	0.647

Table 4. *Cont.*

	>HC to NH$_2$ (Å) of LC	>HC to C=O (Å) of LC	Cu to NH$_2$ (Å) of LC	Cu to O=C< (Å) of LC	Cu to >S=O(Å) of CuSO$_4$ (Avg)	Cu to Cl (Å) of CuCl$_2$ (Avg)	Cu to O=N (Å) of Cu(NO$_3$)$_2$ (Avg)	−C=O..Cu..NH$_2$ (Å) for LC with Cu^{2+} (Avg)	Ionic charge of Cu^{2+}
LC⊃CuCl$_2$	1.487	1.244	2.029	2.296	–	2.246	–	2.162	0.410
[LC-Au] ⊃ CuCl$_2$	1.488	1.245	2.014	2.307	–	2.249	–	2.160	0.414
Cu(NO$_3$)$_2$	–	–	–	–	–	–	2.015	–	0.938
LC⊃Cu(NO$_3$)$_2$	1.489	1.246	2.008	2.254	–	–	2.177	2.131	0.689
[LC-Au] ⊃Cu(NO$_3$)$_2$	1.489	1.243	2.029	2.414	–	–	2.162	2.233	0.689

Table 5. DFT-calculated selected bond angles (in degrees) for the selected parameters of LC; LC-Au; CuSO$_4$; CuCl$_2$; and Cu(NO$_3$)$_2$ their complex **(1:1)** at the ωB97XD/LANL2DZ level of theory in the water solvent system.

	Selected Bond Angles (in Degrees).					
	O=C−CH−NH$_2$	O=S=O (CuSO$_4$)	O–Cu–O	−C=O—Cu–NH$_2$−	Cl−Cu−Cl	O=N=O (Avg.)
LC	109.94	–	–	–	–	–
CuSO$_4$	–	88.81	79.07	–	–	–
LC⊃CuSO$_4$	107.15	92.28	77.61	82.70		
[LC-Au] ⊃CuSO$_4$	107.13	92.39	77.52	82.75	–	–
CuCl$_2$	–	–	–	–	117.47	–
LC⊃CuCl$_2$	108.39	–	–	77.83	149.26	–
[LC-Au] ⊃ CuCl$_2$	108.07	–	–	–	148.51	–
Cu(NO$_3$)$_2$	–	–	66.24	78.89	–	111.22
LC⊃Cu(NO$_3$)$_2$	–	–	60.68	78.89	–	112.61
[LC-Au] ⊃Cu(NO$_3$)$_2$	–	–	61.22	74.59	–	111.51

The DFT analysis shows that the closest distance for the CuSO$_4$ complex is with LC via the bidentate-N,O coordination mode and has the closest distance when compared with the corresponding distances for the LC with Cu(NO$_3$)$_2$) and CuCl$_2$. The central Cu^{2+} has three nearest oxygen atoms and one nearest nitrogen atom at 1.963 ± 0.009 Å (Cu^{2+}-O=S< for coordination with SO$_4{}^{2-}$); 2.006 Å (Cu^{2+}-O=C< for coordination with LC) and 2.022 Å (Cu^{2+}-NH$_2$ for coordination with LC), respectively, for the CuSO$_4$ complex with LC. This finding is consistent with the fact that CuSO$_4$ has higher electronic binding interaction energies (ΔIE) and Gibbs interaction energies (ΔG) with LC than both Cu(NO$_3$)$_2$) and CuCl$_2$ (summarized in Tables 2 and 3).

Figure 5 shows the molecular electrostatic surface potentials [43–46] of LC and their hypothetical 1:1 complexes with CuSO$_4$, CuCl$_2$, and Cu(NO$_3$)$_2$. The surfaces were formed by mapping the electrostatic potentials (MESPs) onto their highest occupied molecular orbital (HOMO) electron density surfaces. The ESPs show the relative polarities and thus the reactive sites of the species: the negative ESP are shown in red and the order of the increasing electrostatic potentials (i.e., highest -ve value) is red > orange > yellow > green > blue.
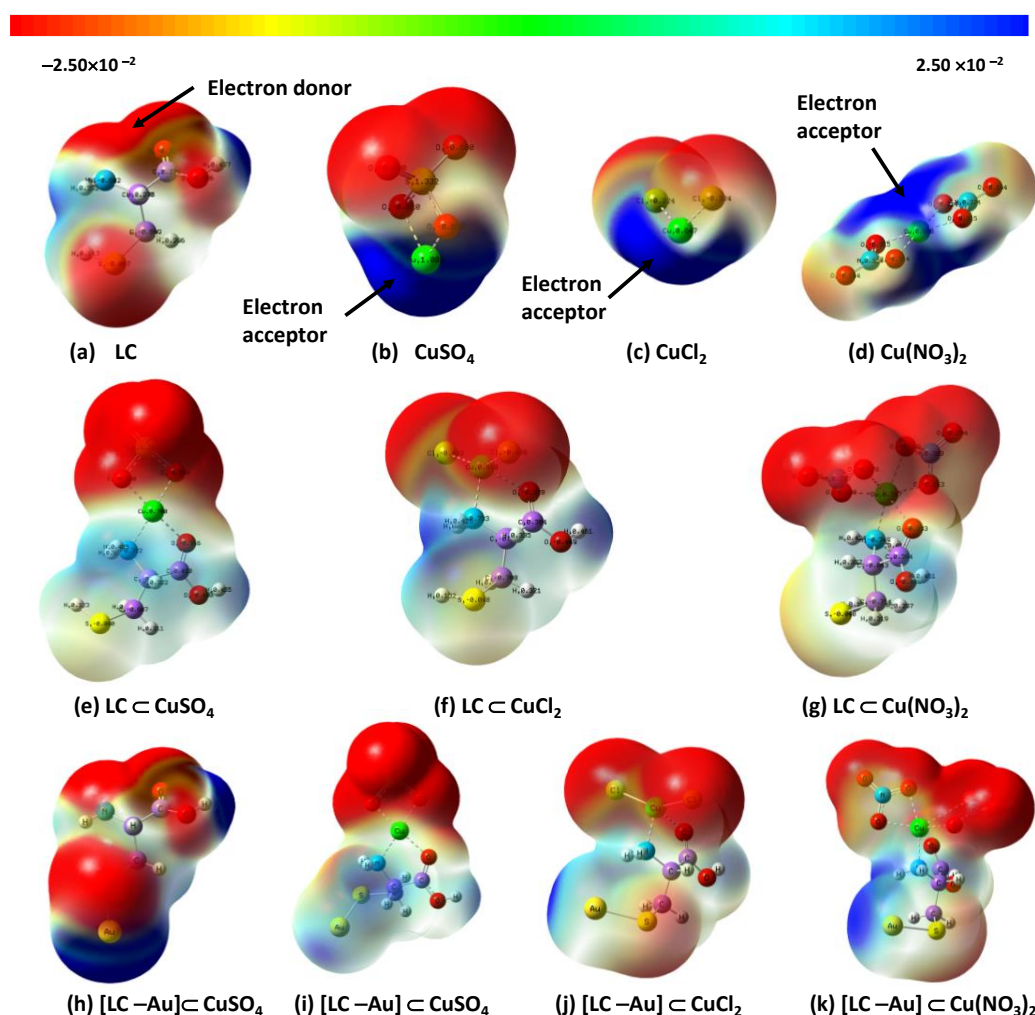
Figure 5. Optimized gas phase molecular structures, ESPs, lowest unoccupied molecular orbital (LUMO), and HOMO structures of (**a**) LC, (**b**) $CuSO_4$; (**c**) $CuCl_2$; (**d**) $Cu(NO_3)_2$; (**e**) $LC \supset CuSO_4$; (**f**) $LC \supset CuCl_2$; (**g**) $LC \supset Cu(NO_3)_2$; (**h**) [LC-Au]; (**i**) $[LC\text{-}Au] \supset CuSO_4$; (**j**) $[LC\text{-}Au] \supset CuCl_2$; and (**k**) $[LC\text{-}Au] \supset Cu(NO_3)_2$ at the ωB97XD/LANL2DZ level of theory in the water solvent system. Color code: carbon = purple, nitrogen = blue; oxygen = red; copper = green; chlorine = yellow-green; sulfur = yellow; gold (Au) = orange, and hydrogen atoms = white.

4. Conclusions

In the present study, we have shown that LC is a suitable receptor molecule which can be used to form a stable SAM onto the gold surfaces of QTFs and is capable of detecting aqueous Cu^{2+} ions in concentrations from 10^{-6} to 10^{-12} M. Only minute sample sizes in the range of 100 μL are needed. Among the Cu^{2+} salts tested, the sulfate counterions had the largest effect upon the QTF responses, as determined by the frequency shifts, in the following order: $SO_4^{2-} > Cl^- > NO_3^-$. The lower limit of detection for Cu^{2+} ions was in the 10^{-12} M range in water solutions. Finally, the DFT-calculated electrostatic electronic interaction energies in all cases were consistent with the experimental results, which supported our hypothetical binding modes for the interaction between the analytes ($CuSO_4$, $CuCl_2$, and $Cu(NO_3)_2$) and the LC SAMs on Au$-$QTFs' sensing surfaces. From Figure 5, ESP clearly demonstrates that the nitrogen atom of the NH_2 group of the LC and the carbonyl oxygen (C=O) atom of the LC both possess significant electron densities, as shown in red, and are the most preferred sites for apparent electrophilic binding, with the nucleophilic partially positive charged Cu^{2+} (blue color) of the $CuSO_4$, $CuCl_2$, and $Cu(NO_3)_2$ analytes. As can also be seen, the negative potentials are generated over the

more electronegative oxygen atoms, whereas the Cu^{2+} exhibits a positive potential region (represented by the blue color) in the structures and are located around the nitrogen and oxygen atoms of the LC. The color gradient shown shows the relative range of electron-rich (red) to electron-poor regions (blue) and the more neutral zones (yellow to green).

Our research team is currently working on the detection of transition metal ions to explore the cation's influence by utilizing the QTFs-LC sensor. These findings will be reported in a scientific journal soon.

References

1.   Yoshinari, N.; Kuwamura, N.; Kojima, T.; Konno, T. Development of coordination chemistry with thiol-containing amino acids. *Coord. Chem Rev.* **2023**, *474*, 214857. [CrossRef]
2.   Pearson, R.G. Hard and soft acids and bases. *J. Am. Chem. Soc.* **1963**, *85*, 3533–3539. [CrossRef]
3.   Pearson, R.G.; Songstad, J. Application of the principle of hard and soft acids and bases to organic chemistry. *J. Am. Chem. Soc.* **1967**, *89*, 1827–1836. [CrossRef]
4.   Häkkinen, H. The gold–sulfur interface at the nanoscale. *Nat. Chem.* **2012**, *4*, 443–455. [CrossRef]
5.   Love, J.C.; Estroff, L.A.; Kriebel, J.K.; Nuzzo, R.G.; Whitesides, G.M. Self-assembled monolayers of thiolates on metals as a form of nanotechnology. *Chem. Rev.* **2005**, *105*, 1103–1169. [CrossRef]
6.   Boisselier, E.; Astruc, D. Gold nanoparticles in nanomedicine: Preparations, imaging, diagnostics, therapies and toxicity. *Chem. Soc. Rev.* **2009**, *38*, 1759–1782. [CrossRef]
7.   Xue, Y.; Li, X.; Li, H.; Zhang, W. Quantifying thiol–gold interactions towards the efficient strength control. *Nat. Commun.* **2014**, *5*, 1–9. [CrossRef]
8.   Ruiz, L.M.; Libedinsky, A.; Elorza, A.A. Role of copper on mitochondrial function and metabolism. *Front. Mol. Biosci.* **2021**, *8*, 711227. [CrossRef]
9.   Festa, R.A.; Thiele, D.J. Copper: An essential metal in biology. *Curr. Biol.* **2011**, *21*, R877–R883. [CrossRef]
10. Kodama, H.; Fujisawa, C. Copper metabolism and inherited copper transport disorders: Molecular mechanisms, screening, and treatment. *Metallomics* **2009**, *1*, 42–52. [CrossRef]
11. Członkowska, A.; Litwin, T.; Dusek, P.; Ferenci, P.; Lutsenko, S.; Medici, V.; Rybakowski, J.K.; Weiss, K.H.; Schilsky, M.L. Wilson disease. *Nat. Rev. Dis. Prim.* **2018**, *4*, 1–20. [CrossRef] [PubMed]
12. Menkes, J.H. Menkes disease and Wilson disease: Two sides of the same copper coin Part 1: Menkes disease. *Eur. J. Paediatr. Neurol.* **1999**, *3*, 147–158. [CrossRef] [PubMed]
13. Denoyer, D.; Masaldan, S.; Fontaine, S.L.; Cater, M.A. Targeting copper in cancer therapy: 'Copper That Cancer'. *Metallomics* **2015**, *7*, 1459–1476. [CrossRef] [PubMed]
14. Strecker, D.; Mierzecki, A.; Radomska, K. Copper levels in patients with rheumatoid arthritis. *Ann. Agric. Environ. Med.* **2013**, *20*, 312–316. [PubMed]

15. Waggoner, D.J.; Bartnikas, T.B.; Gitlin, J.D. The role of copper in neurodegenerative disease. *Neurobiol. Dis.* **1999**, *6*, 221–230. [CrossRef] [PubMed]

16. Gao, J.; Yin, J.; Tao, Z.; Liu, Y.; Lin, X.; Deng, J.; Wang, S. An ultrasensitive fluorescence sensor with simple operation for Cu^{2+} specific detection in drinking water. *ACS Omega* **2018**, *3*, 3045–3050. [CrossRef]

17. Guerrini, L.; Alvarez-Puebla, R.A. Surface-enhanced Raman scattering sensing of transition metal ions in waters. *ACS Omega* **2021**, *6*, 1054–1063. [CrossRef]

18. Feist, B.; Mikula, B.; Pytlakowska, K.; Puzio, B.; Buhl, F. Determination of heavy metals by ICP-OES and F-AAS after preconcentration with 2,20-bipyridyl and erythrosine. *J. Hazard. Mater.* **2008**, *152*, 1122–1129. [CrossRef]

19. Yuhana-Ariffin, E.; Sulaiman, S.S.; Abdul Kadir Jilani, N.; Nokarajoo, D.; Abdul Razak, N.H.; Derawi, D.; Hasbullah, S.A. A new sensing material based on tetraaza/SBA15 for rapid detection of copper (II) ion in water. *Membranes* **2022**, *12*, 1152. [CrossRef]

20. Mandal, D.; Banerjee, S. Surface acoustic wave (SAW) sensors: Physics, materials, and applications. *Sensors* **2022**, *22*, 820. [CrossRef]

21. Zheng, C.; Zhu, L.; Wang, J. A review on rapid detection of modified quartz crystal microbalance sensors for food: Contamination, flavour and adulteration. *TrAC Trends Anal. Chem.* **2022**, *157*, 116805. [CrossRef]

22. Xu, X.; Zhang, N.; Brown, G.M.; Thundat, T.G.; Ji, H.F. Ultrasensitive detection of Cu^{2+} using a microcantilever sensor modified with L-cysteine self-assembled monolayer. *Appl. Biochem. Biotechnol.* **2017**, *183*, 555–565. [CrossRef] [PubMed]

23. Vashist, S.K. For a general review on applications of microcantilevers. *J. Nanotechnol.* **2007**, *3*, 1–15. [CrossRef]

24. Georghiou, P.E.; Rahman, S.; Valluru, G.; Dawe, L.N.; Rahman, S.M.S.; Alodhayb, A.N.; Beaulieu, L.Y. Synthesis of an upper-and lower-rim functionalized calix [4] arene for detecting calcium ions using a microcantilever sensor. *New J. Chem.* **2013**, *37*, 1298–1301. [CrossRef]

25. Valluru, G.; Rahman, S.; Georghiou, P.E.; Dawe, L.N.; Alodhayb, A.N.; Beaulieu, L.Y. Synthesis of a cone-conformer bimodal Calix [4] arene-crown-5 which forms a sensitive cesium ion sensing layer on gold-coated microcantilevers. *New J. Chem.* **2014**, *38*, 5868–5872. [CrossRef]

26. Alodhayb, A.N.; Rahman, S.M.S.; Rahman, S.; Valluru, G.; Georghiou, P.E.; Beaulieu, L.Y. Detection of calcium ions using gold-coated micro-cantilever sensors using upper-and lower-rim functionalized calix [4] arenes. *Sens. Actuators B Chem.* **2014**, *203*, 766773. [CrossRef]

27. Alodhayb, A.N.; Braim, M.; Beaulieu, L.Y.; Valluru, G.; Rahman, S.; Oraby, A.K.; Georghiou, P.E. Metal ion binding properties of a bimodal triazolyl-functionalized Calix [4] arene on a multi-array microcantilever system. Synthesis, fluorescence and DFT computation studies. *RSC Adv.* **2016**, *6*, 4387–4396. [CrossRef]

28. Alodhayb, A.N.; Rahman, S.M.S.; Rahman, S.; Georghiou, P.E.; Beaulieu, L.Y. A 16-microcantilever array sensing system for the rapid and simultaneous detection of the analyte. *Sens. Actuators B Chem.* **2016**, *237*, 459–469. [CrossRef]

29. Al-Gawati, M.A.; Alhazaa, A.; Albrithen, H.; Alnofiay, J.; Alodhayb, A. Effect of surface patterning using femtosecond laser on micromechanical and structural properties of micromechanical sensors. *Mater. Res. Express* **2020**, *7*, 085904. [CrossRef]

30. Aloraini, D.A.; Almuqrin, A.H.; Alanazi, A.; Ain, Q.T.; Alodhayb, A.N. Rapid and sensitive detection of severe acute respiratory syndrome coronavirus 2 in a label-free manner using micromechanical sensors. *Sensors* **2021**, *21*, 4439. [CrossRef]

31. Eliyahu, D.; Gileadi, E.; Galun, E.; Eliaz, N. Atomic force microscope-based meniscus-confined three-dimensional electrodeposition. *Adv Mater Technol.* **2020**, *5*, 1900827. [CrossRef]

32. Barbic, M.; Eliason, L.; Ranshaw, J. Femto-Newton force sensitivity quartz tuning fork sensor. *Sens. Actuators A Phys.* **2007**, *136*, 564–566. [CrossRef]

33. Jahng, J.; Kwon, H.; Lee, E.S. Photo-induced force microscopy by using a quartz tuning-fork sensor. *Sensors* **2019**, *19*, 1530. [CrossRef] [PubMed]

34. Günther, P.; Fischer, U.C.; Dransfeld, K. Scanning near-field acoustic microscopy. *Appl. Phys. B Laser Opt.* **1989**, *48*, 89–92. [CrossRef]

35. Ma, Y.; Hu, Y.; Qiao, S.; Lang, Z.; Liu, X.; He, Y.; Spagnolo, V. Quartz tuning forks resonance frequency matching for laser spectroscopy sensing. *Photoacoustics* **2022**, *25*, 100329. [CrossRef]

36. Alodhayb, A. Quartz tuning fork, a low-cost orthogonal measurement tool for the characterization of low-volume liquid reagents. *Measurement* **2020**, *152*, 107313. [CrossRef]

37. Alshammari, A.; Aldosari, F.; Qarmalah, N.B.; Lsloum, A.; Muthuramamoorthy, M.; Alodhayb, A. Detection of chemical host-guest interactions using a quartz tuning fork sensing system. *IEEE Sens. J.* **2020**, *20*, 12543–12551. [CrossRef]

38. Assaifan, A.K.; Hezam, M.; Al-Gawati, M.A.; Alzahrani, K.E.; Alswieleh, A.; Arunachalam, P.; Al-Mayouf, A.; Alodhayb, A.; Albrithen, H. Label-free and simple detection of trace Pb(II) in tap water using non-Faradaic impedimetric sensors. *Sens. Actuators A Phys.* **2021**, *329*, 112833. [CrossRef]

39. Dennington, R.; Keith, T.A.; Millam, J. GaussView, Version 6.0.16. Semichem Inc.: Shawnee Mission, KS, USA, 2019.

40. Frisch, M.J.; Trucks, G.W.; Schlegel, H.B.; Scuseria, G.E.; Robb, M.A.; Cheeseman, J.R.; Scalmani, G.; Barone, V.; Petersson, G.A.; Nakatsuji, H.; et al. *Gaussian 16, Revision C.01*; Gaussian, Inc.: Wallingford, CT, USA, 2019.

41. Boys, S.; Bernardi, F. The calculation of small molecular interactions by the differences of separate total energies. Some procedures with reduced errors. *Mol. Phys.* **1970**, *19*, 553–566. [CrossRef]

42. Kestner, N.R.; Combariza, J.E. Basis set superposition errors: Theory and practice. In *Reviews in Computational Chemistry*; Wiley-VCH, John Wiley and Sons, Inc.: New York, NY, USA, 1999; Volume 13, p. 99. [CrossRef]

43. Murray, J.S.; Politzer, P. The electrostatic potential: An overview. *Wiley Interdiscip. Rev. Comput. Mol. Sci.* **2011**, *1*, 153–163. [CrossRef]
44. Murray, J.S.; Sen, K. *Molecular Electrostatic Potentials, Concepts and Applications*; Elsevier: Amsterdam, The Netherlands, 1996. [CrossRef]
45. Politzer, P.; Murray, J. The fundamental nature and role of the electrostatic potential in atoms and molecules. *Theor. Chem. Acc.* **2002**, *108*, 134–142. [CrossRef]
46. Yoosefian, M.; Etminan, N. Leucine/Pd-loaded (5,5) single-walled carbon nanotube matrix as a novel nanobiosensors for *in silico* detection of protein. *Amino Acids* **2018**, *50*, 653–661. [CrossRef] [PubMed]